Materials Today Communications 33 (2022) 104946

Contents lists available at ScienceDirect

Materials Today Communications

journal homepage: www.elsevier.com/locate/mtcomm

$NaHCO_3$ assisted multifunctional Co_3O_4, CuO and Mn_2O_3 nanoparticles for tartrazine removal from synthetic wastewater and biological activities

Bushra Zafar [a], Syed Salman Shafqat [b], Muhammad Nadeem Zafar [c,*,1], Sajjad Haider [d], Sajjad Hussain Sumrra [c], Muhammad Zubair [c], Norah Alwadai [e], Fwzah H. Alshammari [f], Amani Saleh Almuslem [g], Muhammad Saeed Akhtar [h]

[a] Department of Chemistry and Forensics, Nottingham Trent University, Nottingham NG11 8NS, UK
[b] Department of Chemistry, Division of Science & Technology, University of Education, Lahore 54770, Pakistan
[c] Department of Chemistry, University of Gujrat, Gujrat 50700, Pakistan
[d] Chemical Engineering Department, College of Engineering, King Saud University, P.O.Box 800, Riyadh 11421, Saudi Arabia
[e] Department of Physics, College of Sciences, Princess Nourah bint Abdulrahman University (PNU), Riyadh 11671, Saudi Arabia
[f] Department of Physics, University College at Nairiyah, University of Hafr Al Batin (UHB), Hafr Al Batin 31981, Saudi Arabia
[g] Department of Physics, College of Science, King Faisal University, Al-Ahsa 31982, Saudi Arabia
[h] School of Chemical Engineering, Yeungnam University, Gyeongsan 38541, Republic of Korea

ARTICLE INFO

Keywords:
Multifunctional metal nanoparticles
Tartrazine
Adsorption, Antioxidant activity
Antimicrobial activity

ABSTRACT

Wastewater treatment as well as biological activities require efficient and cost-effective alternative materials which motivates the interest of scientists for different types of nanomaterials. Nanomaterials are the best class of materials which can be used as adsorbents to treat wastewater and equally can be utilized as antioxidant, antimicrobial agents. The present study involves the synthesis of metal oxide nanoparticles (Co_3O_4, CuO and Mn_2O_3 NPs) by hydrothermal approach followed by thermal decomposition of their respective metal carbonates at their scrupulous decomposition temperature. The prepared NPs were characterized using scanning electron microscopy (SEM), thermogravimetric analysis (TGA) and X-ray diffraction (XRD). The porous, spherical/irregular texture of prepared NPs was confirmed by SEM. Further, XRD analysis validated the formation of smaller size crystals of pure Co_3O_4, CuO and Mn_2O_3 NPs. Thermal stability of as prepared Co_3O_4, CuO and Mn_2O_3 NPs was investigated by TGA. The adsorptive behaviour of all the three NPs was investigated against the removal of an azo dye tartrazine (TZ). The optimum conditions for TZ removal were investigated using well established adsorption parameter like pH, shaking speed, temperature, initial TZ concentration and contact time. The maximum Langmuir adsorption capacity of TZ onto Co_3O_4, CuO and Mn_2O_3 NPs was found to be 204.3, 184.7 and 177.6 mg/g respectively. Langmuir, Freundlich and Temkin adsorption isotherms were applied to TZ adsorption data and results indicated that the Freundlich model was best fitted having higher correlation factor (r^2) indicating multilayer adsorption. Kinetic studies revealed that TZ adsorption onto all three NPs was better descried by pseudo-second-order (PSO) kinetic model. Antimicrobial nature of Co_3O_4, CuO and Mn_2O_3 NPs was studied against fungal and bacterial strains via disk diffusion method and CuO NPs were found with highest inhibition (31 mm and 20 mm) against *Staphylococcus aureus* and *Candida albicans*. Antioxidant behaviour of Co_3O_4, CuO and Mn_2O_3 NPs was observed against DPPH (2, 2-diphenyl-1-picrylhydrazyl) radical and highest inhibition (66%) of Co_3O_4 was observed as compared to Mn_2O_3, CuO. In short, these multifunctional NPs can be used for pollutant removal and equally can be utilised for biological activities.

1. Introduction

Urbanization and industrial development have greatly affected the living beings, whereas the discovery of ideal water treatment technology and antimicrobial agents is still a challenge to the scientists [1,2]. Azo dyes containing (-N═N-) functional group are widely used in textile,

* Corresponding author.
E-mail addresses: nadeem.zafar@uog.edu.pk, znadeempk@gmail.com (M.N. Zafar).
[1] ORCID ID: 0000-0002-2109-7601

https://doi.org/10.1016/j.mtcomm.2022.104946
Received 6 September 2022; Received in revised form 4 November 2022; Accepted 14 November 2022
Available online 15 November 2022

food processing and drug industries, when released in water cause water pollution. Azo dyes have complex aromatic structure and are generally resistant to light, temperature, and oxidizers. These characteristic features make these dyes non-degradable and therefore causes bioaccumulation in living organisms, leading to severe diseases and disorders. Tartrazine (TZ) is an acidic azo dye (Fig. S1) and a well-known food colorant present in drinks and jellies. Tartrazine has some toxic effects and is life-threatening as it can cause cancer and respiratory problems including asthma, so such pollutants must be removed from the water to reduce the pollution of water [3,4].

The removal of the toxic dyes from wastewaters is an essential aspect and has drawn the attention of many research groups globally. Various physical and chemical approaches have been solely or synergistically employed for wastewater treatment such as sedimentation [5], coagulation [6], ultrasonication [7], ozonation [8], membrane separation [9], photocatalysis [10], and adsorption [11] etc. Nevertheless, adsorption route is the most essential technique for the removal of persistent and non-degradable pollutants from wastewater as it is more ecological and economically superior over other techniques [12]. Among various adsorbents, nanomaterials had gained much attention in the field of adsorption due to their exceptional characteristics of small size, enhanced surface area and improved porosity [13]. Many researchers have reported widespread applications of metallic oxide nanoparticles (NPs) in the fields of adsorption, antimicrobial activities [14], bio sensing [15], optical [16] and catalysis [17]. Among various approaches employed to prepare metal oxide NPs, the hydrothermal/thermal decomposition process is more desirable. This method is simple, requires inexpensive materials and has control over the crystallite size and the morphology of NPs. Various metal nanoparticles have been reported using these methods [18–20]. It is worth mentioning that the hydrothermal route assists the formation of metal carbonates leading to the thermal decomposition of carbonates with evolution of CO_2 gas resulting in the formation of porous metal oxide NPs [21]. With the evolution of nanotechnology, metal oxide NPs have also gained consideration as antimicrobial agents due to their broad inhibitory spectrum against bacteria, fungi, and virus [22]. Metal oxide NPs can put forth their impact on microbial cells by causing membrane damage, and injury to proteins and DNA [23]. NPs have also been reported as antioxidant agents; they scavenge the free radicals and provide evidence for the generation of free radicals in the human body by chemiluminescence method [24]. Various nanomaterials have been utilized as adsorbents to remove dyes from contaminated water [25–29] as well as antioxidant/antimicrobial agents [30–32]. Regardless of extensive research on nanomaterials for pollutants removal and biological activities, still researchers are in hunt of highly efficient, low cost, versatile, and novel nanomaterials for the said applications.

In the present study, $NaHCO_3$ assisted Co_3O_4, CuO and Mn_2O_3 NPs were synthesized via hydrothermal route. These prepared NPs were further used as adsorbents for the removal of yellow coloured TZ dye from aqueous media as well as their antimicrobial and antioxidant activities were tested against bacterial/fungal strains and 2,2-diphenyl-1-picrylhydrazyl (DPPH) respectively. The adsorption process was optimized by applying well established adsorption parameters. Experimental data obtained during adsorption process were used to investigate the adsorption process by studying reaction kinetics and adsorption isotherms along with the antioxidant and antimicrobial studies of Co_3O_4, CuO and Mn_2O_3 NPs.

2. Materials and methods

2.1. Materials

Analytical grade cobalt chloride ($CoCl_2 0.6\ H_2O$), copper chloride ($CuCl_2 0.2\ H_2O$), manganese chloride ($MnCl_2 0.6\ H_2O$), and sodium bicarbonate ($NaHCO_3$) were supplied by Sigma Aldrich. Pure TZ dye for adsorption studies was received as gift from University of Agriculture Faisalabad, Pakistan. Methanol, ammonium sulphate (NH_4SO_4), glucose, calcium sulphate ($CuSO_4$) magnesium sulphate ($MgSO_4$), potassium dihydrogen phosphate (KH_2PO_4), and 2,2-diphenyl-1-picrylhydrazyl (DPPH) were supplied by Acros Organics. Different bacterial and fungal strains for antimicrobial activities and antioxidant reagents for antioxidant activities were used. All the reagents and solvents used in the present study were pure (99%) and used without any further purification.

2.2. Preparation of Co_3O_4, CuO and Mn_2O_3 NPs

Co_3O_4, CuO and Mn_2O_3 NPs were prepared using hydrothermal approach. Aqueous solution of each metal salt (20.9 mmol) was prepared while stirring at 700 rpm and 69.2 mmol solution of $NaHCO_3$ was slowly added to each metal solution separately [2]. The solutions were transferred into autoclave for sterilisation and were placed in electric oven for 30 min at 200°C. The metal carbonate solutions were centrifuged to get rid of water and then dried overnight at 60°C. The dried metal carbonates were heated to decompose at their decomposition temperatures, 550°C for Mn_2O_3, 335°C for Co_3O_4 and 290°C for CuO in the muffle furnace for 1 h. Metal oxide NPs (Co_3O_4, CuO and Mn_2O_3) were obtained with the emission of CO_2 gas. The synthesis of these NPs have been reported through thermal decompositions [18,20] and here we used a different strategy to synthesize the NPs with $NaHCO_3$ as the precursor.

2.3. Characterization of Co_3O_4, CuO and Mn_2O_3 NPs

The particles size and morphology of Co_3O_4, CuO and Mn_2O_3 NPs were examined using SEM micrographs obtained from JSM-5910 scanning electron microscope (JEOL, Tokyo, Japan). Crystallite sizes of Co_3O_4, CuO and Mn_2O_3 NPs were investigated by X-ray diffraction (XRD) patterns obtained using PANalytical X′ Pert PRO 3040/60 x-ray diffractometer (Almelo, The Netherland) containing CuKα source at 45 kV and 40 mA. Weight loss patterns of Co_3O_4, CuO and Mn_2O_3 were observed by TGA curves obtained from Universal V4.7 A TA instrument using temperature range from 0 °C to 1000 °C at a heating rate of 10 °C/min for 40 min. InoLab pH 720 (WTW, Weilheim, Germany) was used for pH measurements. UV/Vis spectrophotometer (UV 4000 MRI, Germany) was used to record the ansorbance of TZ in the media before and after treatment with adsorbents (Co_3O_4, CuO and Mn_2O_3 NPs).

2.4. Batch adsorption studies

Batch adsorption approach was adopted to achieve the optimum conditions of well-established adsorption parameters for the removal of TZ from aqueous media. Known quantities of NPs (Co_3O_4, CuO and Mn_2O_3) were added in 100 ppm solutions of TZ separately. Each mixture was shaken mechanically at a constant speed of 150 rpm using an incubator shaker (Heidolph Duomax 1000, USA). The samples were withdrawn after the establishment of equilibrium and thereafter the solutions were centrifuged to separate adsorbents (Co_3O_4, CuO and Mn_2O_3 NPs). The residual amount of TZ in the supernatant was recorded at 425 nm with a double beam spectrophotometer.

The factors like initial TZ concentration (20–120 mg/L), contact time (5–90 min), pH change (2−12), shaking speed (25–200 rpm), and temperature (30–60°C) were studied. The adsorption capacity (the quantity of TZ dye adsorbed on NPs was calculated using equation 1:

$$\text{Adsorption Capacity}(Q_{TZ}) = \frac{C_i - C}{m} \times V \quad (1)$$

where C_i is the initial TZ concentration, C is the equilibrium TZ concentration, V is the volume of TZ solution, and m is the mass of NPs.

Percentage (%) removal of TZ removal was calculated using equation 2:

$$\text{Percentage removal}\left(RE_{TZ}\quad(\%)\right) = \frac{C_i - C}{C_i} \times 100 \qquad (2)$$

2.5. Protocol of antimicrobial activity

The antimicrobial activities of as prepared metallic oxide NPs (Co_3O_4, CuO and Mn_2O_3) were evaluated against bacterial and fungal strains using disc diffusion protocol. For antibacterial activity, *Staphylococcus. Aureus*, *Pseudomonas syringae*, *Streptococcus pyogenes* and *Escherichia coli* and for antifungal activity, *Candida albicans*, *Aspergillus niger* and *Aspergillus fumigatus* were selected. Broth for antibacterial activities was prepared using 5.0 g peptone, 3.0 g yeast, and 1000 mL distilled H_2O. Solutions of HCl/NaOH were used to adjust pH value at 7. The prepared solutions were autoclaved and transferred into petri dishes and allowed to set. The bacterial strains were inoculated and then NPs as well as reference standard drug 'ampicillin' were loaded on paper discs and placed on the inoculum. The Petri dishes were wrapped and incubated at 37°C for 48 h. After 48 h the zones of inhibition were measured to check the antibacterial behaviour of Co_3O_4, CuO and Mn_2O_3 NPs [33].

The media for antifungal activity were prepared using 0.02 g ammonium sulphate, 2.0 g glucose, 0.005 g calcium sulphate, 0.005 g magnesium sulphate, 0.02 g potassium dihydrogen phosphate, and 2.0 g agar per 100 mL of distilled water. The prepared media were autoclaved and then poured into petri dishes to solidify. The fungal strains were spread onto the media and NPs samples along with standard drug were added on paper discs set on the media. The petri dishes were wrapped and incubated at 37°C for 48 h. After 48 h, the zones of inhibition were measured to check the antifungal behaviour of NPs [34].

2.6. Protocol of antioxidant activity

The antioxidant potential (% scavenging) of prepared Co_3O_4, CuO and Mn_2O_3 NPs was evaluated against methanolic 2, 2-diphenyl-1-hydrazyl (DPPH) radical, and concentration of 2000 μM [35]. Five different volume (50–250 μL) of each Co_3O_4, CuO and Mn_2O_3 NPs were prepared separately. The sizeable amount of DPPH solution was added, and solutions were kept in darkness for 30 min. The change in colour of solutions from purple to yellowish after incubating for 30 min was measured using UV/VIS spectrophotometer at 520 nm [36]. Butyl hydroxyl Toluene (BHT) was used as reference standard to compare the radical scavenging. All the tests were performed in triplicate and results obtained were interpreted as percentage scavenging according to equation 3:

$$\text{Percentage scavenging} = \frac{AbsC - AbsS}{AbsC} \times 100 \qquad (3)$$

where AbsC and AbsS are the absorbance of control and sample respectively.

3. Results and discussion

3.1. Characterization of Co_3O_4, CuO and Mn_2O_3 NPs

The crystal structures of Co_3O_4, CuO and Mn_2O_3 NPs were investigated by XRD spectroscopy and results are presented in Fig. 1. The mean crystallite size of Co_3O_4, CuO and Mn_2O_3 NPs was computed using Debye–Scherrer equation. XRD pattern of as prepared Mn_2O_3 NPs was matched with orthorhombic Mn_2O_3 (JCPDS card 73–1826) [37] having mean crystallite size 31.90 nm. The peaks in XRD analysis of Co_3O_4 NPs prepared by thermal decomposition of $CoCO_3$ were in complete agreement with the standard patterns matches of cubic Co_3O_4 (JCPDS 42–1467) [38] having the average crystallite size of 18.27 nm. All reflections in XRD spectrum of CuO NPs readily indexed to monoclinic CuO (JCPDS 48–1548) [39] and the crystallite size calculated was found to be 27.36 nm. No reflections related to any impurities were observed in XRD patterns of Co_3O_4, CuO and Mn_2O_3 NPs. The XRD analysis

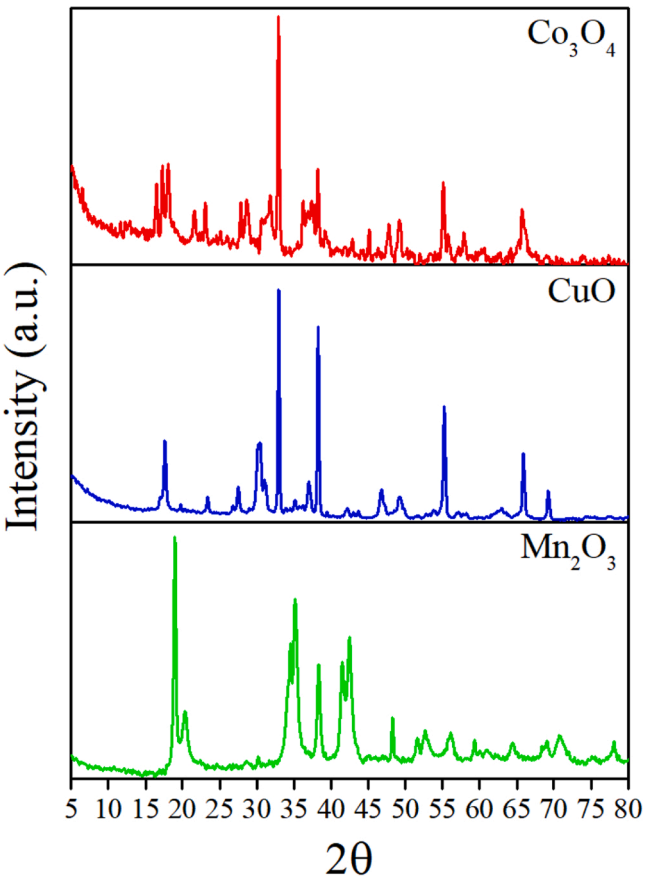

Fig. 1. XRD analysis of Co_3O_4, CuO, and Mn_2O_3 NPs.

confirms the formation of Co_3O_4, CuO and Mn_2O_3 NPs predominantly having smaller sized crystals. In general smaller size material has high surface area which can be suitable for adsorptive studies and antimicrobial applications [40,41].

The morphology and size of as prepared NPs was determined using SEM images shown in Fig. 2. The SEM micrograph of Mn_2O_3 NPs (Fig. 2C) demonstrated that aggregation of considerable number of spherical NPs in the form of big globular submicron's. The porous spherical morphology of the Mn_2O_3 NPs may be attributed to the release of a large amount of CO_2 from $MnCO_3$ resulting in pores development in the sample [37]. Most of the particles of Co_3O_4 (Fig. 2A) were distributed in nano and micro sizes and were interlinked to form an irregular arrangement. The particles were nearly spheroids and were not very compactly packed with each other. There were visible spaces in the arrangement of particles and morphology was somehow an irregular array of nano and lots of microparticles. Some of the particles acquired the shape of flowers which may be attributed to the partial calcination of Co_3O_4, [42]. The SEM image of CuO NPs (Fig. 2B) exhibited a large interparticle porosity and form large agglomerates of NPs. It can be observed that CuO NPs formed have an irregular planar structure with no distinct morphology [43]. Further particle size distribution histograms for Co_3O_4, CuO and Mn_2O_3 NPs were constructed from SEM images and presented in Fig. S2. From the Fig. S2, it can be observed that most of the particles for all NPs were of smaller size and less than 300 nm.

The thermal stability of as-prepared Co_3O_4, CuO and Mn_2O_3 NPs was determined by TGA using temperature range from 0 °C to 1000 °C at a heating rate of 10 °C/min for 40 min. The TGA curve of Mn_2O_3 NPs (Fig. 3a) revealed a very small weight loss and Mn_2O_3 was stable up to 895°C. A further rise in the temperature over 900°C converted Mn_2O_3 to Mn_3O_4 with gradual weight loss from 99.9% to 91.84% and this

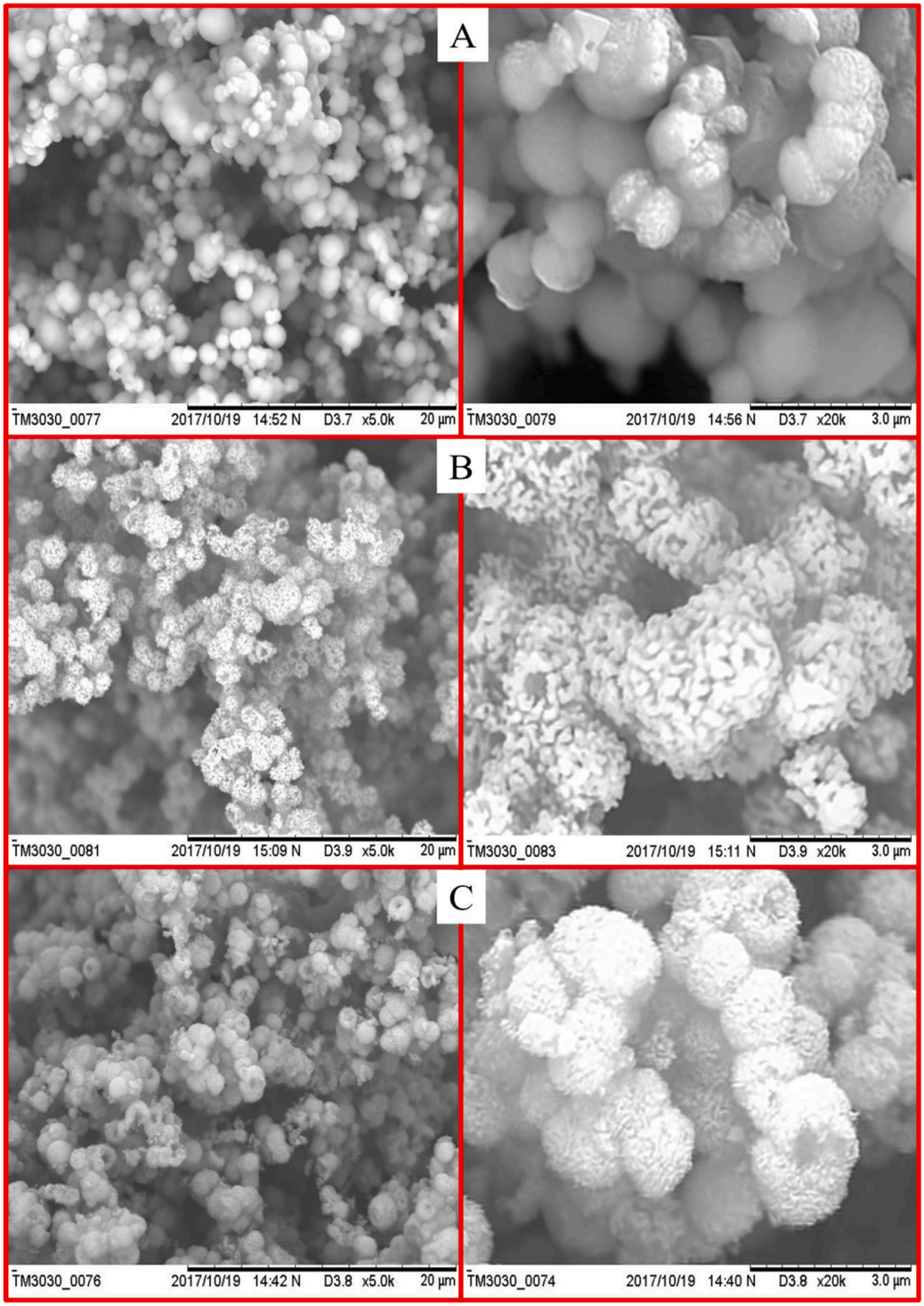

Fig. 2. SEM images of (A) Co_3O_4, (B) CuO, and (C) Mn_2O_3 NPs.

observation agreed well with the literature [44]. TGA curve for Co_3O_4 (Fig. 3b) exhibited a prominent weight loss (6.6%) below 100 °C. This weight loss may be attributed to removal of adsorbed solvent/moisture. From 100 °C onwards, the sample had a high stability of the speel structure with a very small weight loss up to 917 °C. However, between 917 °C and 925 °C there was a weight loss of 28.07%, related to the phase transition of Co_3O_4 to CoO [38]. Fig. 3c shows the TGA curves of CuO NPs. The TGA curve of CuO depicted that 14% weight loss was

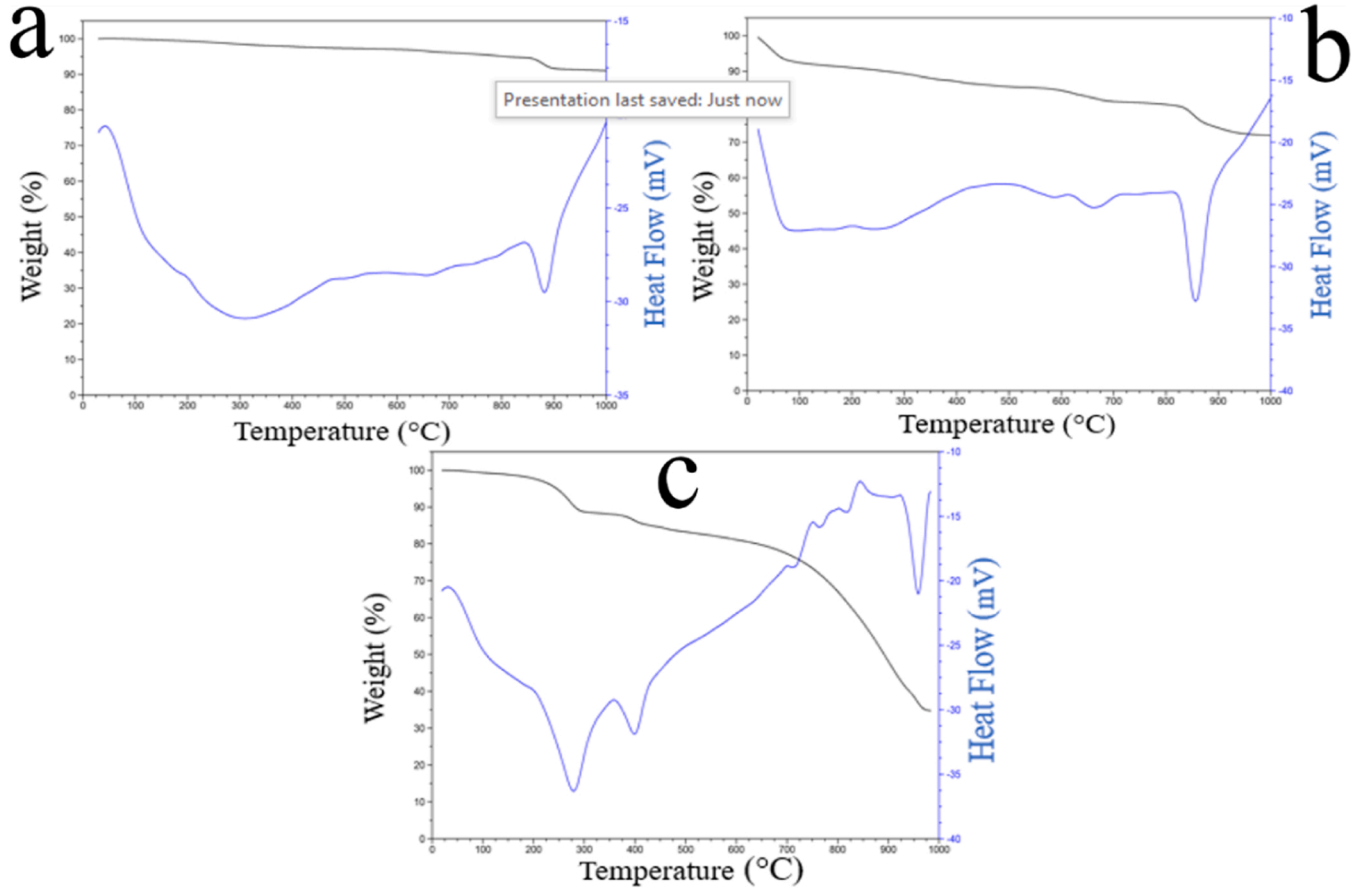

Fig. 3. TGA and DSC analysis of (a) Mn_2O_3, (b) Co_3O_4, and (c) CuO NPs.

observed between 30 and 250 °C, due to water evaporation and nearly 34.80% weight loss was observed at 250–900 °C corresponding to phase transition [45]. The results obtained from TGA confirms that CuO-NPs decomposed more prominently as compared to Mn_2O_3-NPsand Co_3O_4 NPs.

DSC is particularly used as a tool to observe phase transition of materials with variation in temperature. The area of the peak in DSC curve is proportional to the enthalpy and DCS curves of Co_3O_4, CuO and Mn_2O_3 NPs are presented in Fig. 3. An endothermic peak below 100 °C observed in case of Mn_2O_3 was related to the evaporation of moisture as well as solvents. Another endothermic curve at 900 °C attributed to the conversion of Mn_2O_3 to Mn_3O_4 [44]. DSC curve of Co_3O_4 exhibited an endothermic peak below 100 °C which was attributed to the evaporation phenomenon. An endothermic peak observed at 860 °C was evidence towards the formation of crystalline particles and an exothermic peak at 917 °C supported the crystallinity with phase-chemical purity. DSC curve of CuO exhibited two endothermic peaks between 200 and 400 °C, which were attributed to the effect of evaporation and one peak between 900 and 1000 °C confirming the formation of crystalline particles [46].

3.2. Adsorption studies of TZ onto Co_3O_4, CuO and Mn_2O_3 NPs

3.2.1. Effect of pH

The PZC values of Co_3O_4, CuO and Mn_2O_3 NPs were found in the range of 6.5–7.0, which indicated that NPs are positively charged at $pH<pH_{PZC}$ and negatively charged at $pH>pH_{PZC}$. Adsorption rate is greatly affected by pH due to its influence on the binding sites of the adsorbent (NPs) and the adsorbate (TZ). The pH affects the apparent charge of the adsorbent surface and extent of adsorption of adsorbate onto adsorbent based on intermolecular attraction between NPs and TZ molecules. The influence of pH change on adsorption ability of Co_3O_4, CuO and Mn_2O_3 NPs was scrutinized by changing the pH from 2 to 12 and the results are depicted in Fig. 4a. It was observed that the TZ removal efficiency was maximum under acidic conditions. The maximum TZ removal percentage onto Co_3O_4 and Mn_2O_3 was found to be 98% at pH = 2 and 77% at pH = 4 respectively whereas the percentage removal of TZ onto CuO was found to be 88% at pH = 6. It can be noticed from Fig. 4a that the removal efficiency of TZ onto Co_3O_4 not much affected till pH 4. Afterwards, on increasing the initial pH towards basic pH, the removal efficiency of TZ decreased and reached at minimum level at pH = 12. Hence the further adsorption study was evaluated at pH = 4 for Mn_2O_3-NPs, and Co_3O_4-NPs and at pH = 6 for CuO-NPs.

The pH effect can be explained in terms of PZC values of Co_3O_4, CuO and Mn_2O_3 NPs. The PZC values were in the range of 6.5–7.0 and TZ was converted to its corresponding anionic form in aqueous media (Equation 4) [47]. Under acidic pH conditions, (i) Co_3O_4, CuO and Mn_2O_3 NPs got protonated to develop positive charges on the surface (Equation 5) [48] and (ii) at pH < 6.5–7, the Co_3O_4, CuO and Mn_2O_3 NPs were positively charged (pH_{PZC} = 6.5–7.0). So, an effective and strong force of attraction developed between anionic TZ^- and positively charged Co_3O_4, CuO and Mn_2O_3 NPs, which was responsible for high adsorption of TZ at acidic pH (Scheme 1). The decline in adsorption at alkaline pH might be related to the following reasons: (i) as the pH increased, the positive sites on the surface of Co_3O_4, CuO and Mn_2O_3 NPs decreased and further at pH > 6.5–7, the Co_3O_4, CuO and Mn_2O_3 NPs became negatively charged (pH_{PZC} = 6.5–7.0). So, a strong repulsive force developed between negatively charged Co_3O_4, CuO and Mn_2O_3 NPs (Equation 6) and anionic TZ^-, which resulted in sharp decrease in adsorption efficiency (Scheme 1). (ii) at high basic pH, the hydroxyl ions (OH^-) present in abundance, which could compete for active sites on Co_3O_4, CuO and

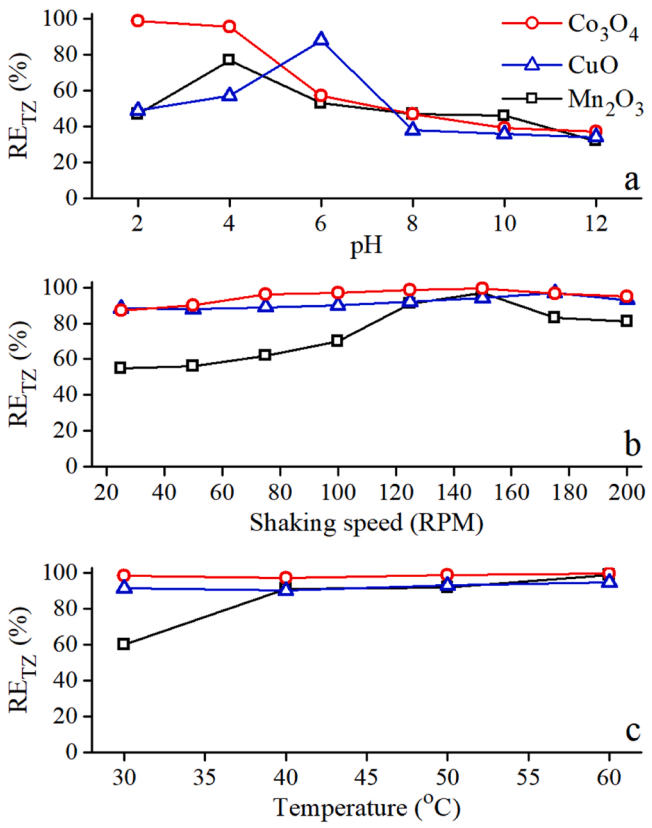

Fig. 4. Effect of pH (a), stirring speed (b) and temperature (c) on adsorption of TZ onto Co_3O_4, CuO and Mn_2O_3 NPs.

Mn_2O_3 NPs [48] with the anionic TZ and the rate of adsorption of TZ droped as can be observed from Fig. 4a.

$$TZNa_3(S) \rightarrow 3Na^+(aq) + TZ^{3-}(aq) \quad (4)$$

$$\text{For pH} < 6.5-7 \quad NPs\text{–}OH + H_3O^+ \rightarrow NPs\text{–}OH_2^+ + H_2O \quad (5)$$

$$\text{For pH} > 6.5-7 \quad NPs\text{–}OH + OH^- \rightarrow NPs\text{–}O^- + H_2O \quad (6)$$

3.2.2. *Effect of shaking speed*

Shaking speed is an imperative factor during adsorption process progression and it helps the TZ molecules to cover up binding sites of NPs for effective adsorption of TZ onto the NPs surface. The influence of shaking speed on uptake of TZ onto NPs (0.4 g/L) was studied using pH 4 for Co_3O_4 and Mn_2O_3 whereas pH 6 for CuO separately, varying shaking speed from 25 to 200 RPM. The results in Fig. 4b showed that percentage removal of TZ onto Mn_2O_3 increased from 55% to 97% when shaking speed increased from 25 to 150 rpm. Similarly, percentage removal of TZ on Co_3O_4 increased from 88% to 99% at speed range from 25 to 150 RPM. Likewise, a similar trend was observed in case of CuO, where percentage removal increased from 88% to 97% when shaking speed increased from 25 to 175 rpm. The increase in percentage removal with increase in shaking speed may be linked to increased collision between TZ molecules and NPs surface resulted in fast electrostatic interactions between NPs and TZ. As clear from the Fig. 4b, at extreme high shaking speeds, a little decrease in percentage removal of TZ on Co_3O_4, CuO and Mn_2O_3 NPs was observed. The possible explanation of this decrease in percentage removal of TZ with increasing shaking speed might be due to desorption of TZ molecules from the surface of at higher RPM.

3.2.3. *Effect of temperature*

Temperature is an essential factor that assists the binding of adsorbate onto adsorbent as temperature helps to overcome the activation energy barrier for a particular reaction. The effect of temperature on

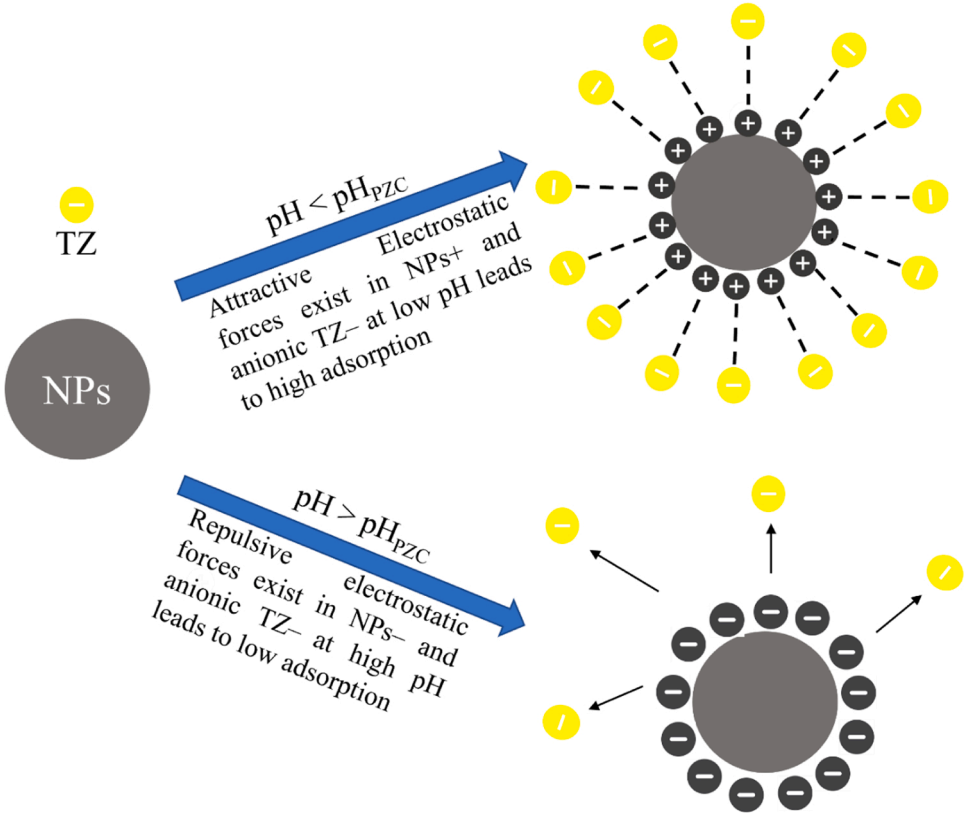

Scheme 1. Possible mechanism and relation of pH with the electrostatic interaction responsible for TZ adsorption onto Co_3O_4, CuO and Mn_2O_3 NPs.

percentage removal of TZ was studied under optimum conditions varying the temperature from 30° to 60 °C. The obtained data (Fig. 4c) revealed that the increase in the temperature of the solutions of TZ from 30° to 50 °C leads to an increase in the adsorption efficiency of TZ onto Co_3O_4, CuO and Mn_2O_3 NPs, which illustrated that the adsorption process is endothermic and chemical in nature. Further increase in temperature till 60 °C, no increase in TZ adsorption efficiency is observed. The increase in removal of TZ onto Co_3O_4, CuO and Mn_2O_3 NPs at higher temperature is due to increasing the number of TZ molecules acquiring sufficient energy to overcome of activation energy, which resulted in availability of more active sites and adsorption process became more favourable. It could also be linked to the increased diffusion and mobility of TZ ions from the bulk solution toward the NPs surface, thereby increasing the number of TZ molecules acquiring sufficient energy to undergo chemical reaction with NPs at higher temperature.

3.2.4. *Equilibrium study and modelling of TZ onto Co_3O_4, CuO and Mn_2O_3 NPs*

The effect of initial TZ concentration was examined at three different temperatures (30, 40 and 50 °C) for Co_3O_4, CuO and Mn_2O_3 NPs. TZ concentration was varied from 20 to 120 ppm using the following experimental conditions (NPs dose 0.4 g/L, pH 4 for Co_3O_4 and Mn_2O_3, pH 6 for CuO). The results shown in Fig. S3 indicated that the retention of TZ increased as the initial TZ concentration increased. Adsorption isotherms were used to show the level of interaction between adsorbents (NPs) and adsorbate (TZ). Langmuir, Freundlich and Temkin models were employed for studying adsorption behaviour at the initial concentration of TZ (20–120 mg/L) at 30,40, and 50 °C temperature.

Langmuir adsorption model explains the monolayer coverage of TZ molecules onto NPs surface leading to homogenous adsorption over the adsorbent surface and Freundlich model explains the multilayer coverage of adsorbent sites by adsorbate, leading to heterogeneous adsorption on the surface of the adsorbent whereas Temkin model also explains the multilayer coverage of the adsorption surface. The non-linear equations of Langmuir, Freundlich and Temkin isotherms [49–51] are provided in supplementary data (Section S1).

The coefficient of determination (r^2) for Langmuir, Freundlich and Temkin isotherms were estimated using non-linear fitting of these models. The Langmuir model rate constant (related to binding sites and affinity of adsorption energy), b_L (L/g) and theoretical adsorption capacity, Q_T (mg/g) were calculated using non-linear fitting of Langmuir model (Fig. S4-S6), the Freundlich constant, K_F ((mg/g)(mg/L)$^{1/n}$) and adsorption intensity, 1/n were estimated from non-linear fitting of Freundlich model (Fig. S4-S6) whereas Temkin constants, b_T and K_T (L/mg) (belongs to equilibrium binding constant and heat of adsorption respectively) were calculated from non-linear fitting of Temkin model (Fig. S4-S6).

The values of all isotherm's parameters and r^2 are tabulated in Table 1. The r^2 values obtained from all three models reflected that the adsorption of TZ onto Co_3O_4, CuO and Mn_2O_3 NPs at 30, 40 and 50 °C was fitted with these models in the following order, Freundlich (0.941–0.977) > Langmuir (0.884–0.922) > Temkin (0.779–0.866). The greater r^2 values obtained by fitting the Freundlich model revealed that this model was best fitted to describe the mechanism of TZ adsorption onto Co_3O_4, CuO and Mn_2O_3 NPs at 30, 40, and 50 °C. These findings proved a multilayer adsorption of TZ onto heterogeneous surface of NPs. Further the estimated values of adsorption intensity (n = 2.937 – 3.420) were less than 10 indicating the suitable adsorption of TZ onto Co_3O_4, CuO and Mn_2O_3 NPs (favourable if n is less than 10). Besides, the experimental adsorption capacity (Q) and Langmuir theoretical adsorption capacity (Q_T) were in close agreement demonstrating suitable adsorption of TZ. Further the higher values of b_T obtained from Temkin model validated a strong interactive force between TZ and Co_3O_4, CuO and Mn_2O_3 NPs whereas positive values of b_T revealed endothermic nature of adsorption process of TZ onto NPs.

A comparative study for the Langmuir adsorption capacities (Q_T) of Co_3O_4, CuO and Mn_2O_3 NPs with other reported adsorbent nanomaterials for TZ was also executed and presented din Table 2. The Q_T for TZ was 204.3, 184.7 and 177.6 mg/g for Co_3O_4, CuO and Mn_2O_3 NPs respectively. It can be observed that adsorption capacity of these NPs for TZ is quite comparable with other available nanomaterials in shorter equilibrium time. The rapid uptake and quick establishment of equilibrium show the efficiency of these NPs for dyes contaminated wastewater treatment.

3.2.5. *Kinetic study of TZ onto Co_3O_4, CuO and Mn_2O_3 NPs*

The TZ adsorption rate onto Co_3O_4, CuO and Mn_2O_3 NPs was studied by observing the influence of contact time from 5 to 90 min under optimized conditions and results are presented in Fig. S7. Fig. S7 illustrated that there was linear increase in adsorption capacity of TZ onto CuO and Mn_2O_3 NPs in first 30 min as 89 and 85 mg/g for CuO and Mn_2O_3 respectively. In contract there was slow rate of adsorption in first 20 min and then a sharp increase in rate of adsorption of TZ onto Co_3O_4 was observed. In first 20 min, the adsorption capacity of TZ onto Co_3O_4

Table 2
Comparison for TZ adsorption by different nanomaterials.

Adsorbent	Q_T (mg/g)	Reference
NPsFeOB	59.79	[25]
Ni-Ag NPs/rGO	26.31	[26]
PLL-Fe_3O_4-(GO-MWCNTs)	775.2	[52]
Fe_3O_4/C/CoAl-LDH	52.30	[53]
PPy/SrM/GO	123.5	[54]
PPy@TN	42.50	[55]
ZnS/CuO-CNT	183.5	[56]
Co_3O_4 NP	204.3	Present study
CuO NP	184.7	
Mn_2O_3NP	177.6	

Table 1
Adsorption isotherms parameters using nonlinear fitting of Langmuir, Freundlich, and Temkin models for Co_3O_4, CuO and Mn_2O_3.

Temperature		Langmuir			Freundlich			Temkin		
	Q	**Q_T**	**b_L**	**r^2**	**K_F**	**n**	**r^2**	**K_T**	**b_T**	**r^2**
	Co_3O_4									
30 °C	171.5	186.5	0.103	0.902	48.93	3.304	0.959	15.78	117.8	0.809
40 °C	178.0	204.3	0.101	0.914	52.79	3.256	0.967	20.11	113.6	0.821
50 °C	176.5	196.8	0.115	0.906	55.04	3.420	0.958	23.80	121.2	0.811
	CuO									
30 °C	168.8	176.7	0.110	0.898	41.63	2.960	0.952	5.807	98.40	0.813
40 °C	173.8	184.7	0.117	0.906	45.90	3.048	0.964	8.046	102.4	0.833
50 °C	178.8	188.1	0.103	0.884	43.62	2.937	0.941	8.281	107.2	0.779
	Mn_2O_3									
30 °C	158.8	162.7	0.112	0.896	40.54	3.118	0.953	6.145	107.2	0.814
40 °C	163.8	177.6	0.107	0.922	42.26	3.007	0.977	5.505	101.0	0.866
50 °C	165.2	175.9	0.112	0.904	44.57	3.149	0.961	8.019	111.7	0.828

Q (Experimental adsorption capacity) = mg g-1; QT (Theoretical adsorption capacity) = mg g-1; KF = [(mg g-1)(mg L-1)1/n]; bL = L mg-1; KT = L g-1; bT = J mol-1

NPs was 55 mg/g, which was increased up to 98 mg/g after 30 min Fig. 5 showed the visual indication of maximum removal of TZ when Co_3O_4 NPs were used under optimization conditions. The colour of TZ solution was yellow before adsorption, changed to almost black after adding Co_3O_4 NPs. The TZ+NPs mixture was stirred for 90 min to ensure equilibrium. It was noted that after adsorption the solution was colourless meaning TZ was almost 95–98% adsorbed by Co_3O_4 NPs.

To further get insights from time vs adsorption capacity experiments, the kinetic models were applied to predict the rate of the adsorption process. For this purpose, two most conventional models pseudo-first order (PFO) and pseudo-second-order (PSO) were applied on kinetics data of TZ adsorption onto Co_3O_4, CuO and Mn_2O_3 NPs [57,58]. The linear forms of both PFO and PSO models are presented in Section S2, which were used to calculate the r^2 values for both PFO and PSO models. The PFO rate constant (K_1) and theoretical adsorption capacity (Q_{t1}) were determined using slope and intercept of linear fitting of PFO model respectively (Fig. 6a) whereas PSO rate constant (K_2) and theoretical adsorption capacity (Q_{t2}) were estimated from intercept and slope of linear fitting of PSO model respectively (Fig. 6b). The calculated parameters from both models are depicted in Table 3.

The most fitted model was chosen based on the values of r^2. From the values given in Table 3, it can be observed that the values of r^2 obtained from PFO model (0.8338, 0.9784 and 0.9048 for Co_3O_4, CuO and Mn_2O_3 NPs respectively) were lower compared to r^2 values obtained from PSO model (0.9615, 0.9990 and 0.9954 for Co_3O_4, CuO and Mn_2O_3 NPs respectively). Further the values of theoretical, Q_{t1} calculated from PFO model were significantly different from the experimental Q_t values whereas the theoretical, Q_{t2} values calculated from PSO model were closer to the experiment obtained values, Q_t. Both these observations suggested that the PFO model did not clarify the kinetics of TZ adsorption instead PSO model displayed a good fit to the experimental data collected for TZ adsorption onto Co_3O_4, CuO and Mn_2O_3 NPs. The dependence of TZ adsorption with PSO model indicated that the rate limiting step for TZ adsorption onto Co_3O_4, CuO and Mn_2O_3 NPs was chemical adsorption. Moreover, the PSO rate constants values were lower ($K_2 = 0.0006$, 0.0029 and 0.0015 for Co_3O_4, CuO and Mn_2O_3 NPs respectively), which suggested that there was lesser competition of surface sites for adsorption at lower TZ concentration.

The diffusion mechanism cannot be explained well with PFO and PSO models. So, to understand the adsorption mechanism, the intra-particle diffusion model (IpD) was applied to experimental data of TZ adsorption onto Co_3O_4, CuO and Mn_2O_3 NPs. The equation of this IpD model is presented in Section S2. The values of IpD rate constant, K_i and

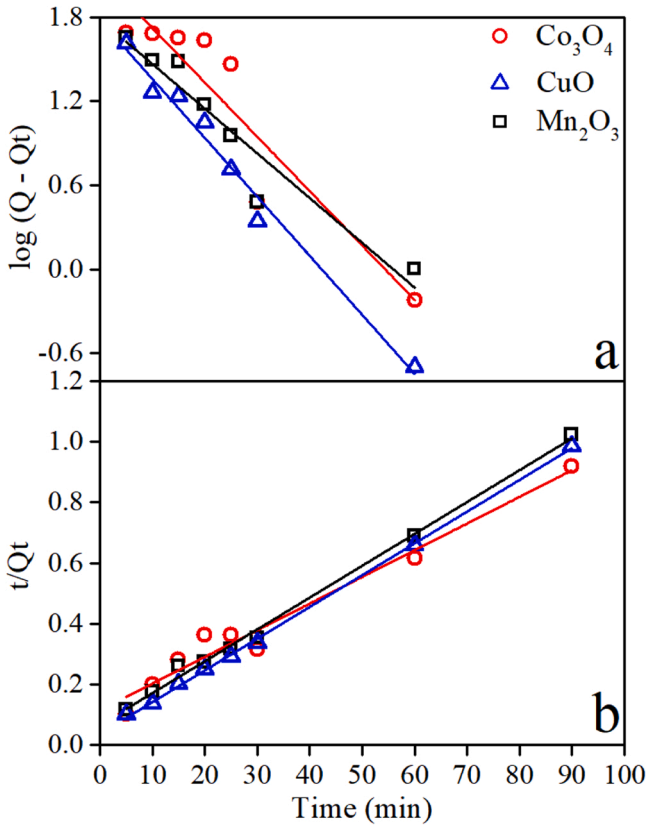

Fig. 6. PFO (a) and PSO (b) models applied on TZ adsorption data using Co_3O_4, CuO and Mn_2O_3 NPs.

Z were estimated from the slope and intercept of the plot between Q_t and $t^{1/2}$ (Fig. 7) and summarized in Table 3. The higher values of Z for all NPs indicated the predominant effect of boundary layer. The IpD model plot shown in Fig. 7 indicated multi linearity, two linear regions for CuO and Mn_2O_3 whereas three linear regions for Co_3O_4. This multi linearity suggested that the adsorption process of TZ was governed by more than one process. The 1st region in plot for CuO and Mn_2O_3 indicated prompt diffusion stage/external surface adsorption where a huge amount of TZ was swiftly adsorbed on the exterior surface of CuO and Mn_2O_3 NPs. The 2nd region in plot for CuO and Mn_2O_3 represented a slow adsorption

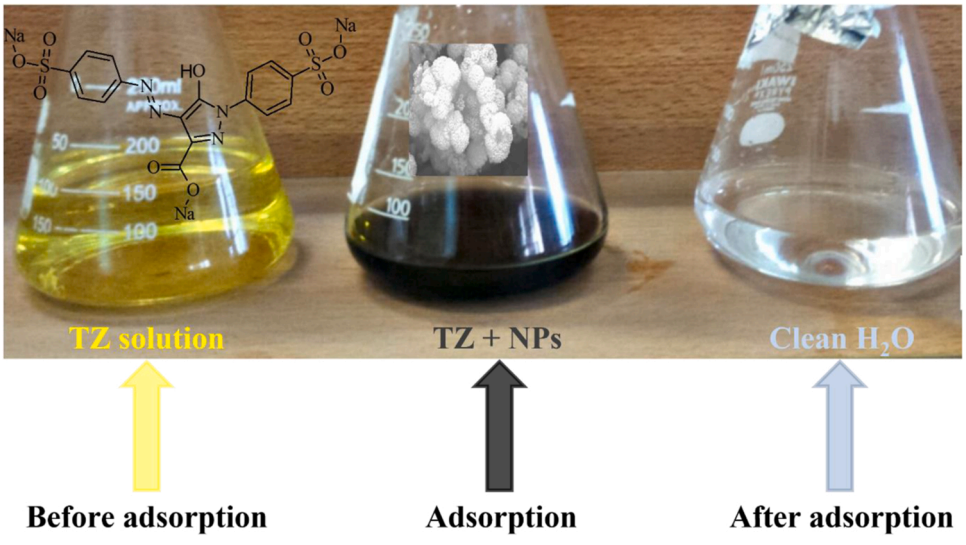

Fig. 5. Visual observation of TZ removal using Co_3O_4 NPs under optimized conditions.

Table 3
Pseudo first and second order kinetic model's parameters for TZ dye adsorption onto Co_3O_4, CuO and Mn_2O_3.

Models		Parameters	Values		
		Adsorbents →	**Co_3O_4**	**CuO**	**Mn_2O_3**
Pseudo 1st order		Qt_1 (mg g^{-1})	129.4	60.48	61.18
		K_1 (min^{-1})	0.0875	0.0967	0.0735
		r^2	0.8338	0.9784	0.9048
Experimental		Qt (mg g^{-1})	98.00	91.20	88.00
Pseudo 2nd order		Qt_2 (mg g^{-1})	114.9	96.15	100.0
		K_2 (g mg^{-1} min^{-1})	0.0006	0.0029	0.0015
		r^2	0.9615	0.9990	0.9954
Intraparticle diffusion	Region I	K_i (mg g^{-1} $min^{-0.5}$)	2.768	11.05	12.95
		C	42.24	30.72	13.46
	Region II	K_i (mg g^{-1} $min^{-0.5}$)	-124.1	0.565	0.755
		C	39.56	86.12	80.95
	Region III	K_i (mg g^{-1} $min^{-0.5}$)	0.763	–	–
		C	91.02	–	–

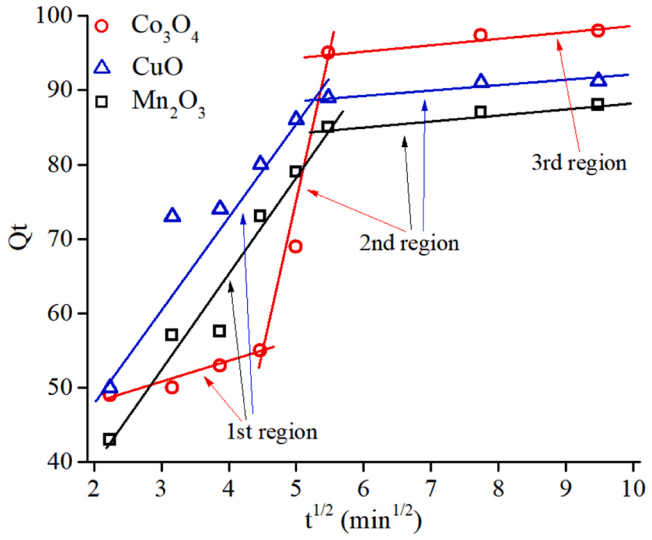

Fig. 7. IpD model applied on TZ adsorption data using Co_3O_4, CuO and Mn_2O_3 NPs as adsorbents.

stage which was related to IpD of TZ within the pores of CuO and Mn_2O_3 adsorbents. In contrast, the movement of TZ from bulk to Co_3O_4 surface can be described in three consecutive steps: (a) external surface/diffusion, shipping TZ to the external Co_3O_4 surface, (b) intraparticle/internal diffusion, transporting TZ to the interior portion of Co_3O_4, (c) the TZ adsorbed onto active sites of Co_3O_4. Three processes were involved in adsorption of TZ onto Co_3O_4 and that might be the reason of higher adsorption of TZ onto Co_3O_4. Additionally, the linear lines in IpD plots of Co_3O_4, CuO and Mn_2O_3 NPs did not pass through the origin. This observation revealed that the IpD control step was not the only rate controlling step but other mechanism pathways were also involved during TZ adsorption process onto Co_3O_4, CuO and Mn_2O_3 NPs [59,60].

3.2.6. Thermodynamic study

To observe the effect of temperature on removal of TZ onto Co_3O_4, CuO and Mn_2O_3 NPs while increasing the TZ initial concentration, the experiments were performed at three temperatures viz 30, 40 and 50 °C. Results shown in Fig. S3 revealed that the adsorption capacity for TZ increased with the increase of TZ initial concentration and became slightly higher at higher temperature from 30° to 50 °C. These observations indicated that adsorption of TZ on Co_3O_4, CuO and Mn_2O_3 NPs was an endothermic chemisorption process.

To confirm above process and to endorse the nature and feasibility of adsorption process of TZ, thermodynamic parameters [free energy change (ΔG°), enthalpy (ΔH) and entropy (ΔS)] were important to estimate. The equations used to calculate these parameters are presented in Section S3. The values of ΔS and ΔH were estimated from the intercept and slope of the plot between K_d and 1/T (Fig. S8) whereas the values of ΔG° were determined by equation 7 (Section 3). The dimensionless K_d values were estimated using the method described in [61], first by converting the Langmuir constant (L mg^{-1}) into L mol^{-1} and then using the following equation 7.

$$K_d = 55.51\left(\text{mol } L^{-1}\right) \times b_L \times 1000 \times \text{molecular weight of TZ} \quad (7)$$

The calculated values of parameters are summarised in Table 4. The negative values of ΔG° on all temperature revealed a spontaneous nature of adsorption process of TZ onto Co_3O_4, CuO and Mn_2O_3 NPs whereas positive values of ΔS and ΔH for all Co_3O_4, CuO and Mn_2O_3 NPs indicated that the adsorption of TZ is dominant by chemical sorption and endothermic in nature. Furthermore, ΔG° values were increased as the temperature increases reflecting TZ adsorption process was more promising at higher temperature.

3.3. Biological activities of Co_3O_4, CuO and Mn_2O_3 NPs

3.3.1. Antioxidant activity

The prepared Co_3O_4, CuO and Mn_2O_3 NPs were screened for antioxidant potential against methanolic DPPH radical (2000 μM) in-vitro assay. Evaluation of results revealed that the percentage of radical inhibition was observed 66%, 27% and 11% against Co_3O_4, CuO and Mn_2O_3, respectively (Fig. 8) when a NPs concentration of 250 μL was used. The maximum radical inhibition potential shown by Co_3O_4 was 66% at 250 μL concentration whereas remaining concentrations (<250 μL) showed less inhibition of DPPH radical. In comparison of all three NPs, the minimum radical scavenging activity was shown by Mn_2O_3 as 1.05% at 50 μL. Butyl hydoxy toluene (BHT), a synthetic antioxidant with best approved scavenging was used as reference standard to compare the activities of NPs. In comparison of NPs and BHT, the later showed almost 100% scavenging with all the equivalent concentrations employed for evaluation of antioxidant potential. These results confirmed that Co_3O_4, CuO and Mn_2O_3 NPs has the antioxidant activity potential and further work needed to make efficient NPs that can be actively used as antioxidant agents in accordance with the previous studies [36]. Further, the modified metal NPs can immobilize some functional groups, which can be beneficial to provide better antioxidant activity [62]. In a study, CeO_3, TiO_2 and Fe_3O_4 NPs have been found for their excellent antioxidant effect. Transition metals could exhibit a high tolerance for reversible oxidation/reduction due to the oxidation states therefore, metal-based NPs, could offer the exceptional antioxidant effects [63]. In another research the antioxidant activity of silver NPs with DPPH scavenging was reported as 29.55% [64]. Results of present research are reasonably attractive in respect of antioxidant potential of NPs preferably Co_3O_4 with better activity among the constructed NPs.

Table 4
Thermodynamics parameters for TZ dye onto Co_3O_4, CuO and Mn_2O_3.

Parameters	Temperature	Co_3O_4	CuO	Mn_2O_3
ΔH (kJ mol^{-1})		1.419	3.312	1.414
ΔS (J mol^{-1} K^{-1})		132.9	137.7	131.4
ΔG° (kJ mol^{-1})	30 °C	-37.62	-37.78	-37.83
	40 °C	-38.81	-39.19	-38.96
	50 °C	-40.40	-40.10	-40.32

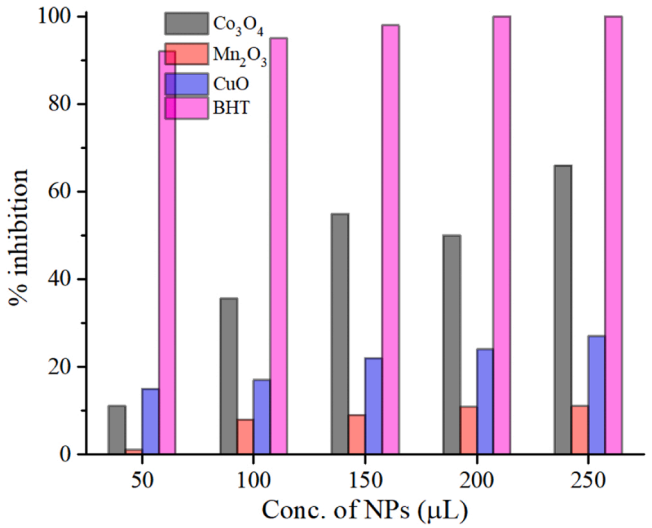

Fig. 8. Antioxidant assay ((% DDPH radical scavenging) of Co_3O_4, CuO and Mn_2O_3 NPs using various concentrations.

3.3.2. Antibacterial activity

The antibacterial potential of $NaHCO_3$ assisted Co_3O_4, CuO and Mn_2O_3 NPs was determined by applying well reported and certified disk diffusion method. Four different bacterial strains named as *E. Coli, S. Aureus, P. Syringae,* and *S. Pyogenes* were used whereas ampicillin was used as positive control against the bacterial strains. The results of NPs antibacterial activity are shown in Fig. 9a, and disc diffusion experiments are shown in Fig. S9. The results indicated that although all three Co_3O_4, CuO and Mn_2O_3 NPs were found to have less antibacterial activity compared to the positive control ampicillin, but it is apparent from the results that these NPs have the potential of antibacterial activity against bacterial strains used in this study. Comparison of antibacterial activity of Mn_2O_3, Co_3O_4, and CuO NPs showed that CuO NPs had relatively better antibacterial activity against bacterial strains *E. Coli, S. Aureus,* and *S. Pyogenes* and maximum activity (31 mm) was observed against bacterial strain, *S. Aureus* in accordance with previous studies [33]. Mn_2O_3 NPs displayed a similar trend of inhibitory activity (23, 25, 27 mm for *E. Coli, P. Syringae,* and *S. Aureus* respectively) but did not develop any inhibition against *S. Pyogenes*. Co_3O_4 NPs also inhibited all the bacterial strains with a moderate inhibition activity against *E. Coli, S. Aureus,* and *S. Pyogenes* but the high activity (26 mm) against the *P. Syringae* strain compared to Co_3O_4, and Mn_2O_3 NPs. Overall, the results suggest that CuO NPs behave with stronger antimicrobial impact against the bacterial strains than Co_3O_4, and Mn_2O_3 NPs.

Metal-based NPs have non-specific bacterial toxicity mechanisms and usually they have no binding relation to a specific receptor in the bacterial cell, which develop the resistance difficulty in bacteria to improve the antibacterial activity of NPs. Many types of metal-based NPs (Ag, Au, CuO, ZnO) were evaluated against gram-positive and gram-negative bacteria, which had shown promising results [65]. In the present research, CuO NPs has shown the comparable potential of antibacterial activity in comparison to the nanomaterials reported in literature. Shankar et al., synthesized ZnO, CuO, and Ag NPs to evaluate their efficacy against the bacterial strains and their results showed a significant antibacterial potential especially CuO NPs against bacterial strains [66]. In another research, the antimicrobial property of CuO NPs was applied against gram negative *E. coli* and *P. vulgaris* and gram positive *S. aureus* pathogens, which has revealed interesting results of inhibition at different concentrations of CuO NPs [67].

3.3.3. Antifungal activity

In parallel to evaluation of antibacterial activity, Co_3O_4, CuO and Mn_2O_3 NPs were also tested against the fungal strains named *C. albicans*,

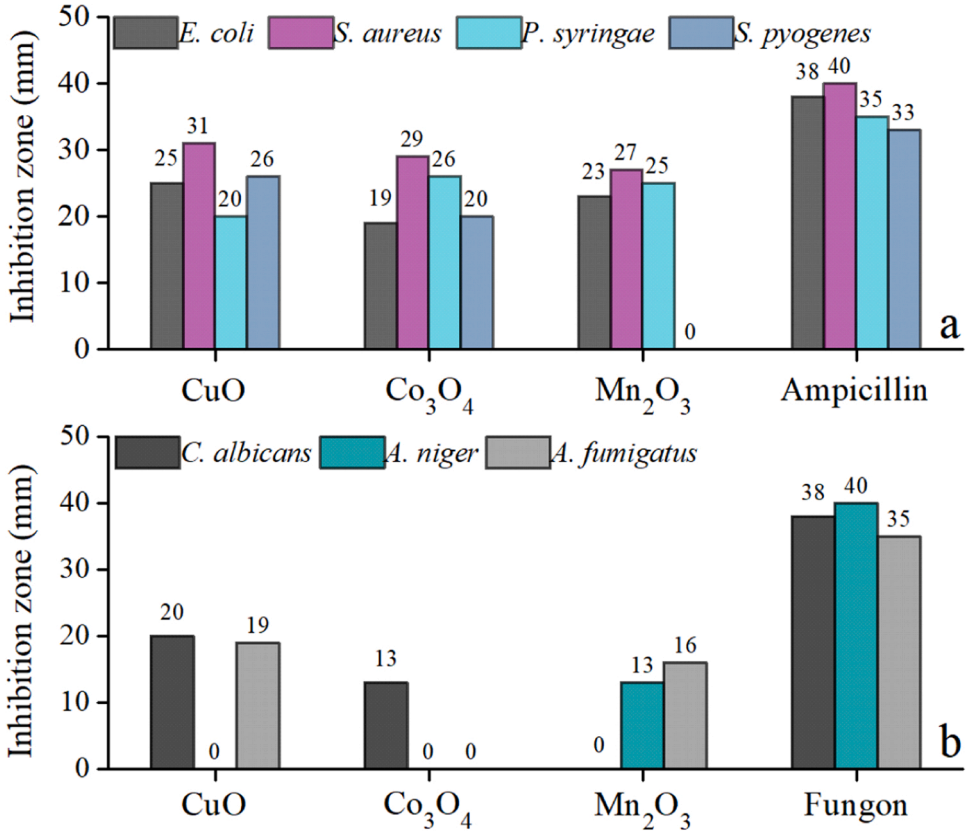

Fig. 9. Antibacterial (a) and antifungal (b) activities of Co_3O_4, CuO and Mn_2O_3 NPs using different bacterial and fungal strains.

A. niger, and *A. fumigatus*. The antifungal activity results are depicted in Fig. 9b, and disc diffusion experiments are shown in Fig. S10. From the results it can be clearly observed that Co_3O_4, CuO and Mn_2O_3 NPs had not shown very high activity against all fungal strains as compared to positive control. However, the small antifungal activity shown by Co_3O_4, CuO and Mn_2O_3 NPs is providing a hypothesis that NPs can be an alternate if their activity can be enhanced by different means such as modification with different moieties or synthesis through greener approach etc. Among the Co_3O_4, CuO and Mn_2O_3 NPs, the high activity was observed against *C. albicans* (20 mm) with CuO NPs. Additionally, CuO had shown inhibition activity against *C. albicans*, and *A. fumigatus* and zero activity towards *A. niger*. Co_3O_4 NPs had shown activity only against *C. albicans* whereas Mn_2O_3 had shown activity against fungal strains *A. niger*, and *A. fumigatus* and no activity against *C. albicans*. CuO had shown maximum antifungal activity among the prepared NPs and the results were compared and found in accordance with literature [68, 69]. Based on activity shown by Co_3O_4, CuO and Mn_2O_3 NPs against fungal species it may be suggested that more work is needed to improve the activity of metal oxide for real applications.

Many metal NPs have been investigated as antifungal agents, such as Se, Ni, Mg, Pd, and Fe and different methods of synthesis have been used to produce these NPs with different shapes and sizes, which may enhance antifungal activities. As aforementioned, shape, structure, and size of the NPs play an important role in antifungal activity. On the other hand, it has been reported that the concentration of NPs can play an important role in antifungal activity. Further the greener approach to synthesis NPs is better option than chemical methodology [70]. Contrary activities observed for Co_3O_4, CuO and Mn_2O_3 NPs against fungal species in comparison to literature reported activities of NPs of metals, it may be improved by changing method of synthesis, size, shape, concentration in future study.

4. Conclusions

In the current work, $NaHCO_3$ assisted multifunctional Co_3O_4, CuO and Mn_2O_3 NPs were successfully prepared using hydrothermal method, characterized using applicable analytical techniques (XRD, TGA and SEM) and used effectively as adsorbent to remove TZ as well as for antimicrobial and antioxidant activities. XRD analysis revealed the formation of smaller size crystallites metal oxide NPs with high surface area. The SEM images showed the existence of metal oxide NPs in the form large agglomerates having porous spherical/irregular morphology. Among the Co_3O_4, CuO and Mn_2O_3 NPs, the maximum Langmuir adsorption capacity (204.3 mg/g) for TZ was shown by Co_3O_4 NPs under optimum adsorption parameters. The adsorption data was fitted very appropriately with Freundlich model implying the heterogenous nature of adsorption process. The kinetics studies revealed that adsorption processes in case of all the three metallic oxide NPs was followed by PSO model. The antibacterial behaviour of prepared Co_3O_4, CuO and Mn_2O_3 NPs was examined against the pathogenic species *E. coli, S. aureus, P. syringae,* and *S. pyogenes*, and all the NPs showed a considerable potential as antibacterial nano-moieties with CuO having better antibacterial activity. Similarly, antifungal behaviour of Co_3O_4, CuO and Mn_2O_3 NPs was evaluated using fungal strains *C. albicans*, *A. niger* and *A. fumigatus*. Among the Co_3O_4, CuO and Mn_2O_3 NPs, the high activity was observed against *C. albicans* (20 mm) with CuO NPs. Overall, research study revealed that Co_3O_4, CuO and Mn_2O_3 NPs had multifunctional properties that they not only removed TZ from wastewater but also equally useful for biological activities like antioxidant and antimicrobial which was an additional silver lining of the NPs.

CRediT authorship contribution statement

Bushra Zafar: Investigation, Writing - original draft. **Syed Salman Shafqat:** Methodology, Software. **Muhammad Nadeem Zafar:** Conceptualization, Project administration, Supervision. **Sajjad Haider:** Funding acquisition. **Sajjad Hussain Sumrra:** Writing - review & editing. **Muhammad Zubair:** Writing – review & editing. **Norah Alwadai:** Data curation. **Fwzah H. Alshammari:** Writing – review & editing. **Amani Saleh Almuslem:** Formal analysis. **Muhammad Saeed Akhtar:** Validation.

Declaration of Competing Interest

The authors declare that they have no known competing financial interests or personal relationships that could have appeared to influence the work reported in this paper.

Data Availability

Data will be made available on request.

Acknowledgments

The authors acknowledge the Department of Chemistry, University of Gujrat for providing lab facilities. The authors sincerely appreciate funding from the Researchers Supporting Project no. RSP-2021/399, King Saud University, Riyadh, Saudi Arabia.

Appendix A. Supporting information

Supplementary data associated with this article can be found in the online version at doi:10.1016/j.mtcomm.2022.104946.

References

[1] M. Massaro, C.G. Colletti, G. Lazzara, S. Guernelli, R. Noto, S. Riela, Synthesis and characterization of halloysite–cyclodextrin nanosponges for enhanced dyes adsorption, ACS Sustain. Chem. Eng. 5 (2017) 3346–3352.
[2] Q. Li, S. Mahendra, D.Y. Lyon, L. Brunet, M.V. Liga, D. Li, P.J. Alvarez, Antimicrobial nanomaterials for water disinfection and microbial control: potential applications and implications, Water Res. 42 (2008) 4591–4602.
[3] R. Gupta, S. Ranjan, A. Yadav, B. Verma, K. Malhotra, Toxic effects of food colorants erythrosine and tartrazine on zebrafish embryo development, Curr. Res. Nutr. Food Sci. J. 7 (2019) 876–885.
[4] K.A. Amin, F.S. Al-Shehri, Toxicological and safety assessment of tartrazine as a synthetic food additive on health biomarkers: a review, Afr. J. Biotechnol. 17 (2018) 139–149.
[5] I.Z. Sefnides, M. Dwiastuti, Modeling of sedimentation process in water, in: IOP conference series, Journal of Physics: Conference series, IOP Publishing (2018) 012080.
[6] L. Muruganandam, M.P.S. Kumar, A. Jena, S. Gulla, B. Godhwani. Treatment of waste water by coagulation and flocculation using biomaterials, IOP Publishing, 2017, p. 032006.
[7] N.A.H. Fetyan, A.T.M. Salem, Water purification using ultrasound waves: application and challenges, Arab J. Basic Appl. Sci. 27 (2020) 194–207.
[8] C. Wei, F. Zhang, Y. Hu, C. Feng, H. Wu, Ozonation in water treatment: the generation, basic properties of ozone and its practical application, Rev. Chem. Eng. 33 (2017) 49–89.
[9] D. Zioui, Z. Tigrine, H. Aburideh, S. Hout, M. Abbas, N.K. Merzouk, Membrane technology for water treatment applications, Int. J. Chem. Environ. Eng. 6 (2015) 153–157.
[10] L. Lin, W. Jiang, L. Chen, P. Xu, H. Wang, Treatment of produced water with photocatalysis: recent advances, affecting factors and future research prospects, Catalysts 10 (2020) 924.
[11] R. Yousef, H. Qiblawey, M.H. El-Naas, Adsorption as a process for produced water treatment: a review, Processes 8 (2020) 1657.
[12] G. Crini, Recent developments in polysaccharide-based materials used as adsorbents in wastewater treatment, Prog. Polym. Sci. 30 (2005) 38–70.
[13] M.A. Gatoo, S. Naseem, M.Y. Arfat, A. Mahmood Dar, K. Qasim, S. Zubair, Physicochemical properties of nanomaterials: implication in associated toxic manifestations, BioMed Research International, 2014 (2014) Article ID 498420.
[14] A. Mukherjee, I.M. Sadiq, T.C. Prathna, N. Chandrasekaran, Antimicrobial activity of aluminium oxide nanoparticles for potential clinical applications, in: A. Méndez-Vilas (Ed.), Science Against Microbial Pathogens: Communicating Current Research and Technological Advances, Formatex Research Center, Valladolid, Spain, 2011, pp. 245–251.
[15] S. Zeng, K.-T. Yong, I. Roy, X.-Q. Dinh, X. Yu, F. Luan, A review on functionalized gold nanoparticles for biosensing applications, Plasmonics 6 (2011) 491–506.
[16] C.J. Murphy, T.K. Sau, A.M. Gole, C.J. Orendorff, J. Gao, L. Gou, S.E. Hunyadi, T. Li, Anisotropic metal nanoparticles: synthesis, assembly, and optical applications, J. Phys. Chem. B 109 (2005) 13857–13870.

[17] Y. Zhou, C. Jin, Y. Li, W. Shen, Dynamic behavior of metal nanoparticles for catalysis, Nano Today 20 (2018) 101–120.
[18] N.M. Hosny, I. Gomaa, A. Abd El-Moemen, Z.M. Anwar, Adsorption of Ponceau Xylidine dye by synthesised Mn_2O_3 nanoparticles, Int. J. Environ. Anal. Chem. (2021) 1–17.
[19] N.M. Hosny, I. Gomaa, A. Abd El-Moemen, Z.M. Anwar, Synthesis, magnetic and adsorption of dye onto the surface of NiO nanoparticles, J. Mater. Sci.: Mater. Electron. 31 (2020) 8413–8422.
[20] N.M. Hosny, S. Rady, F.I.E. Dossoki, Adsorption of methylene blue onto synthesized Co_3O_4, NiO, CuO and ZnO nanoparticles, J. Iran. Chem. Soc. 19 (2022) 1877–1887.
[21] T. Yang, Z. Huang, Y. Liu, M. Fang, X. Ouyang, M. Hu, Controlled synthesis of porous $FeCO_3$ microspheres and the conversion to α-Fe_2O_3 with unconventional morphology, Ceram. Int. 40 (2014) 11975–11983.
[22] A. Raghunath, E. Perumal, Metal oxide nanoparticles as antimicrobial agents: a promise for the future, Int. J. Antimicrob. Agents 49 (2017) 137–152.
[23] R. Wan, Y. Mo, L. Feng, S. Chien, D.J. Tollerud, Q. Zhang, DNA damage caused by metal nanoparticles: involvement of oxidative stress and activation of ATM, Chem. Res. Toxicol. 25 (2012) 1402–1411.
[24] L. Valgimigli, A. Baschieri, R. Amorati, Antioxidant activity of nanomaterials, J. Mater. Chem. B 6 (2018) 2036–2051.
[25] A.C. de Lima Barizão, M.F. Silva, M. Andrade, F.C. Brito, R.G. Gomes, R. Bergamasco, Green synthesis of iron oxide nanoparticles for tartrazine and bordeaux red dye removal, J. Environ. Chem. Eng. 8 (2020), 103618.
[26] R. Mirzajani, S. Karimi, Ultrasonic assisted synthesis of magnetic Ni-Ag bimetallic nanoparticles supported on reduced graphene oxide for sonochemical simultaneous removal of sunset yellow and tartrazine dyes by response surface optimization: application of derivative spectrophotometry, Ultrason. Sonochem. 50 (2019) 239–250.
[27] P.K. Ngoc, T.K. Mac, H.T. Nguyen, D.T. Viet, T.D. Thanh, P. Van Vinh, B.T. Phan, A. T. Duong, R. Das, Superior organic dye removal by $CoCr_2O_4$ nanoparticles: Adsorption kinetics and isotherm, J. Sci.: Adv. Mater. Devices 7 (2022), 100438.
[28] R. Singh, S. Bokka, A. Kumar Lakshya, A. Chowdhury, CaO-doped tetragonal ZrO_2 nanoparticles as an effective adsorbent for the removal of organic dye waste, Appl. Surf. Sci. 596 (2022), 153651.
[29] V. Jeyavani, S.P. Mukherjee, Crystal phase and morphology-controlled synthesis of tungsten oxide nanostructures for remarkably ultrafast adsorption and separation of organic dyes, Inorg. Chem. 61 (2022) 18119–18134.
[30] T. Riaz, A. Munnwar, T. Shahzadi, M. Zaib, S. Shahid, M. Javed, S. Iqbal, K. Rizwan, M. Waqas, B. Khalid, N.S. Awwad, H.A. Ibrahium, M.A. Bajaber, Phyto-mediated synthesis of nickel oxide (NiO) nanoparticles using leaves' extract of Syzygium cumini for antioxidant and dyes removal studies from wastewater, Inorg. Chem. Commun. 142 (2022), 109656.
[31] A. Wasilewska, U. Klekotka, M. Zambrzycka, G. Zambrowski, I. Święcicka, B. Kalska-Szostko, Physico-chemical properties and antimicrobial activity of silver nanoparticles fabricated by green synthesis, Food Chem. 400 (2023), 133960.
[32] W. Anupong, R. On-uma, K. Jutamas, D. Joshi, S.H. Salmen, T.A. Alahmadi, G. K. Jhanani, Cobalt nanoparticles synthesizing potential of orange peel aqueous extract and their antimicrobial and antioxidant activity, Environ. Res. 216 (2023), 114594.
[33] S. Razmavar, M.A. Abdulla, S.B. Ismail, P. Hassandarvish, Antibacterial activity of leaf extracts of Baeckea frutescens against methicillin-resistant Staphylococcus aureus, BioMed. Res. Int. (2014) (2014). Article ID 521287.
[34] K. Adam, A. Sivropoulou, S. Kokkini, T. Lanaras, M. Arsenakis, Antifungal activities of Origanum vulgare subsp. hirtum, Mentha spicata, Lavandula angustifolia, and Salvia fruticosa essential oils against human pathogenic fungi, J. Agric. Food Chem. 46 (1998) 1739–1745.
[35] Z. Bedlovičová, I. Strapáč, M. Baláž, A. Salayová, A brief overview on antioxidant activity determination of silver nanoparticles, Molecules 25 (2020) 3191.
[36] T.G. Choleva, F.A. Kappi, D.L. Giokas, A.G. Vlessidis, Paper-based assay of antioxidant activity using analyte-mediated on-paper nucleation of gold nanoparticles as colorimetric probes, Anal. Chim. Acta 860 (2015) 61–69.
[37] M.Y. Nassar, A.S. Amin, I.S. Ahmed, S. Abdallah, Sphere-like Mn_2O_3 nanoparticles: facile hydrothermal synthesis and adsorption properties, J. Taiwan Inst. Chem. Eng. 64 (2016) 79–88.
[38] L.J. Cardenas-Flechas, A.M. Raba, J. Barba-Ortega, L.C. Moreno, M.R. Joya, Effect of calcination temperature on the behavior of the agglomerated Co_3O_4 nanoparticles obtained through the Sol–Gel method, J. Inorg. Organomet. Polym. Mater. 31 (2021) 121–128.
[39] N. Nasihat Sheno, A. Morsali, Synthesis of different copper oxide nano-structures from direct thermal decomposition of porous copper (II) metal-organic framework precursors, Int. J. Nanosci. Nanotechnol. 8 (2012) 99–104.
[40] T. Naseem, T. Durrani, The role of some important metal oxide nanoparticles for wastewater and antibacterial applications: A review, Environ. Chem. Ecotoxicol. 3 (2021) 59–75.
[41] K.R. Raghupathi, R.T. Koodali, A.C. Manna, Size-dependent bacterial growth inhibition and mechanism of antibacterial activity of zinc oxide nanoparticles, Langmuir 27 (2011) 4020–4028.
[42] M.R.S.A. Janjua, Synthesis of Co_3O_4 nano aggregates by co-precipitation method and its catalytic and fuel additive applications, Open Chem. 17 (2019) 865–873.
[43] K.J. Arun, A.K. Batra, A. Krishna, K. Bhat, M.D. Aggarwal, P.J.J. Francis, Surfactant free hydrothermal synthesis of copper oxide nanoparticles, Am. J. Mater. Sci. 5 (2015) 36–38.
[44] B. Deljoo, H. Tan, S.L. Suib, M. Aindow, Thermally activated structural transformations in manganese oxide nanoparticles under air and argon atmospheres, J. Mater. Sci. 55 (2020) 7247–7258.
[45] G. Manjari, S. Saran, T. Arun, A.V.B. Rao, S.P. Devipriya, Catalytic and recyclability properties of phytogenic copper oxide nanoparticles derived from Aglaia elaeagnoidea flower extract, J. Saudi Chem. Soc. 21 (2017) 610–618.
[46] J. Díaz-Visurraga, C. Daza, C. Pozo, A. Becerra, C. von Plessing, A. García, Study on antibacterial alginate-stabilized copper nanoparticles by FT-IR and 2D-IR correlation spectroscopy, Int. J. Nanomed. 7 (2012) 3597–3612.
[47] H. Ouassif, E.M. Moujahid, R. Lahkale, R. Sadik, F.Z. Bouragba, Em Sabbar, M. Diouri, Zinc-aluminum layered double hydroxide: high efficient removal by adsorption of tartrazine dye from aqueous solution, Surf. Interfaces 18 (2020), 100401.
[48] H.O. Chukwuemeka-Okorie, F.K. Ekuma, K.G. Akpomie, J.C. Nnaji, A.G. Okereafor, Adsorption of tartrazine and sunset yellow anionic dyes onto activated carbon derived from cassava sievate biomass, Appl. Water Sci. 11 (2021) 27.
[49] I. Langmuir, The adsorption of gases on plane surfaces of glass, mica and platinum, J. Am. Chem. Soc. 40 (1918) 1361–1403.
[50] H.M.F. Freundlich, Over the adsorption in solution, J. Phys. Chem. 57 (1906) 385–470.
[51] M.J. Temkin, V. Pyzhev, Recent modifications to Langmuir isotherms, Acta Physicochim. URSS 12 (1940) 217–225.
[52] D. Hu, X. Wan, X. Li, J. Liu, C. Zhou, Synthesis of water-dispersible poly-l-lysine-functionalized magnetic Fe_3O_4-(GO-MWCNTs) nanocomposite hybrid with a large surface area for high-efficiency removal of tartrazine and Pb(II), Int. J. Biol. Macromol. 105 (2017) 1611–1621.
[53] B. Maryam, Z. Javad, Carbon-magnetic layered double hydroxide as a new nanosorbent for efficient removal of tartrazine and indigo carmine dyes from water solutions; multivariate optimization and adsorption characterization, J. Water Chem. Technol. 44 (2022) 259–268.
[54] S. Ebrahimpoor, V. Kiarostami, M. Khosravi, M. Davallo, A. Ghaedi, Optimization of tartrazine adsorption onto polypyrrole/$SrFe_{12}O_{19}$/graphene oxide nanocomposite using central composite design and bat inspired algorithm with the aid of artificial neural networks, Fibers Polym. 22 (2021) 159–170.
[55] V. Srivastava, P. Maydannik, Y.C. Sharma, M. Sillanpää, Synthesis and application of polypyrrole coated tenorite nanoparticles (PPy@TN) for the removal of the anionic food dye 'tartrazine' and divalent metallic ions viz. Pb(ii), Cd(ii), Zn(ii), Co (ii), Mn(ii) from synthetic wastewater, RSC Adv. 5 (2015) 80829–80843.
[56] E. Sharifpour, P. Arabkhani, F. Sadegh, A. Mousavizadeh, A. Asfaram, In-situ hydrothermal synthesis of CNT decorated by nano ZnS/CuO for simultaneous removal of acid food dyes from binary water samples, Sci. Rep. 12 (2022) 12381.
[57] Y.-S. Ho, G. McKay, Pseudo-second order model for sorption processes, Process Biochem. 34 (1999) 451–465.
[58] S. Lagergren, About the theory of so-called adsorption of soluble substances, K. Sven. Vetensk. Handlngar 24 (1898) 1–39.
[59] L. Fan, C. Luo, X. Li, F. Lu, H. Qiu, M. Sun, Fabrication of novel magnetic chitosan grafted with graphene oxide to enhance adsorption properties for methyl blue, J. Hazard. Mater. 215–216 (2012) 272–279.
[60] A. Maged, S. Kharbish, I.S. Ismael, A. Bhatnagar, Characterization of activated bentonite clay mineral and the mechanisms underlying its sorption for ciprofloxacin from aqueous solution, Environ. Sci. Pollut. Res. 27 (2020) 32980–32997.
[61] E.C. Lima, A. Hosseini-Bandegharaei, J.C. Moreno-Piraján, I. Anastopoulos, A critical review of the estimation of the thermodynamic parameters on adsorption equilibria. Wrong use of equilibrium constant in the Van't Hoof equation for calculation of thermodynamic parameters of adsorption, J. Mol. Liq. 273 (2019) 425–434.
[62] X. Ge, Z. Cao, L. Chu, The antioxidant effect of the metal and metal-oxide nanoparticles, Antioxid. 11 (2022) 791.
[63] A. Bumajdad, J. Eastoe, A. Mathew, Cerium oxide nanoparticles prepared in self-assembled systems, Adv. Colloid Interface Sci. 147–148 (2009) 56–66.
[64] A.K. Keshari, R. Srivastava, P. Singh, V.B. Yadav, G. Nath, Antioxidant and antibacterial activity of silver nanoparticles synthesized by Cestrum nocturnum, J. Ayurveda Integr. Med. 11 (2020) 37–44.
[65] E. Sánchez-López, D. Gomes, G. Esteruelas, L. Bonilla, A.L. Lopez-Machado, R. Galindo, A. Cano, M. Espina, M. Ettcheto, A. Camins, A.M. Silva, A. Durazzo, A. Santini, M.L. Garcia, E.B. Souto, Metal-based nanoparticles as antimicrobial agents: an overview, Nanomaterials 10 (2020) 292.
[66] S. Shankar, J.-W. Rhim, Facile approach for large-scale production of metal and metal oxide nanoparticles and preparation of antibacterial cotton pads, Carbohydr. Polym. 163 (2017) 137–145.
[67] S. Sathiyavimal, S. Vasantharaj, D. Bharathi, M. Saravanan, E. Manikandan, S. S. Kumar, A. Pugazhendhi, Biogenesis of copper oxide nanoparticles (CuONPs) using Sida acuta and their incorporation over cotton fabrics to prevent the pathogenicity of Gram negative and Gram positive bacteria, J. Photochem. Photobiol. B: Biol. 188 (2018) 126–134.
[68] N.-D. Pham, M.-M. Duong, M.-V. Le, H.A. Hoang, Preparation and characterization of antifungal colloidal copper nanoparticles and their antifungal activity against Fusarium oxysporum and Phytophthora capsici, Comptes Rendus Chim. 22 (2019) 786–793.
[69] S.C. Garg, N. Siddiqui, Antifungal activity of some essential oil isolates, Pharmazie 47 (1992) 467–468.
[70] A.R. Cruz-Luna, H. Cruz-Martínez, A. Vásquez-López, D.I. Medina, Metal nanoparticles as novel antifungal agents for sustainable agriculture: current advances and future directions, J. Fungi 7 (2021) 1033.